Gel Polymer Electrolytes Based on Poly(vinylidene fluoride-*co*-hexafluoropropylene) and Salt-Concentrated Electrolytes for High-Voltage Lithium Metal Batteries

Yuta Maeyoshi,[a] Kazuki Yoshii,[a] Hikaru Sano,[a] Hikari Sakaebe,[a,b] Ryota Tamate,[c] Tomoaki Kaneko,[d] and Keitaro Sodeyama[e]*

[a]Research Institute of Electrochemical Energy, Department of Energy and Environment, National Institute of Advanced Industrial Science and Technology (AIST), 1-8-31 Midorigaoka, Ikeda, Osaka 563-8577, Japan

[b]Institute for Materials Chemistry and Engineering, Kyushu University, 6-1 Kasuga koen, Kasuga-shi, Fukuoka 816-8580, Japan

[c]Research Center for Macromolecules & Biomaterials, National Institute for Materials Science (NIMS), 1-2-1 Sengen, Tsukuba, Ibaraki 305-0047, Japan

[d]Department of Computational Science and Technology, Research Organization for Information Science and Technology (RIST), 1-18-16 Hamamatsucho, Minato-ku, Tokyo 105-0013, Japan

[e]Center for Basic Research on Materials, National Institute for Materials Science (NIMS), 1-1 Namiki, Tsukuba, Ibaraki 305-0044, Japan

*Corresponding author:

E-mail: y.maeyoshi@aist.go.jp

ABSTRACT

Although high-voltage lithium (Li) metal batteries are promising next-generation energy storage devices, their practical use is hindered by their poor cycling stability owing to poor electrolyte compatibility with both Li metal anodes and 5 V-class cathodes. In this study, we report that the gelation of salt-concentrated electrolytes with weakly coordinating poly(vinylidene fluoride-*co*-hexafluoropropylene) (PVDF-HFP) effectively improves the cycling stability of high-voltage Li metal batteries. PVDF-HFP-based gel polymer electrolyte with a salt-concentrated electrolyte composed of lithium bis(fluorosulfonyl)amide (LiFSA) and sulfolane (SL) achieves a high Coulombic efficiency and dense deposition morphology of Li metal anodes, along with sufficient oxidation stability against 5 V-class cathodes. Experimental and computational analyses show that the solvation structures of SL–Li^+–FSA^-, similar to those in the original concentrated electrolyte, are maintained in the PVDF-HFP matrix, which leads to the formation of a low-resistance solid electrolyte interphase (SEI) rich in lithium fluoride and sulfur compounds. These findings indicate that the formation of the low-resistance SEI in the gel polymer electrolyte promotes dense Li deposition and suppresses electrolyte decomposition and inactive Li formation, resulting in highly efficient Li metal anodes. We demonstrate that the stable cycling of a high-voltage Li metal battery with a 5 V-class $LiNi_{0.5}Mn_{1.5}O_4$ cathode is enabled by the gel electrolyte, which inhibits the deposition of transition metals dissolved from the cathode onto the anode. This electrolyte and interface

design is an effective strategy for developing 5 V-class Li metal batteries and can be applied to other high-energy-density metal batteries with high-voltage cathodes.

KEYWORDS: salt-concentrated electrolytes, gel polymer electrolytes, lithium metal batteries, lithium metal anodes, high-voltage cathodes, coordination environments, solid electrolyte interphases

1. INTRODUCTION

High-energy-density rechargeable batteries must be developed to achieve a sustainable society based on renewable energy sources such as sunlight and wind. A simple approach to enhance the battery energy density is to elevate the voltage by combining anode and cathode materials with large electrochemical potential gaps and increasing the capacity of these materials. Li metal is an ideal anode material for high-energy-density battery applications owing to its remarkable properties, such as a low electrochemical potential of −3.04 V vs. standard hydrogen electrode and a high theoretical capacity of 3860 mAh g^{-1}. [1] However, Li metal anode applications are hindered by the insufficient Coulombic efficiency (CE) in the Li plating/stripping reactions, which arises from whisker-like Li deposits (so-called Li dendrites) and the reductive decomposition of electrolytes by Li metal. [2] The decomposition of conventional electrolytes comprising $LiPF_6$ and organic carbonates forms a unstable and

heterogeneous solid electrolyte interphase (SEI) on Li metal, which leads to Li whisker growth, promoting further electrolyte decomposition and the formation of inactive Li (so-called dead Li). [2-4] For cathode materials, high-voltage cathodes (such as $LiNi_{0.5}Mn_{1.5}O_4$ and $LiCoPO_4$) have received much attention because of their high operating potential (~5 V vs. Li/Li^+). [5, 6] However, these 5 V-class cathodes have shown poor cycling stability, largely attributed to the oxidative decomposition of electrolytes, degradation of the cathodes, and dissolution of transition metals from the cathodes followed by deposition of these metals on the anodes. [5-9] Thus, electrolytes that can address the abovementioned issues must be developed for high-energy-density batteries with Li metal anodes and 5 V-class cathodes (5 V-class Li metal batteries).

Recently, various electrolytes have been intensively designed and developed to improve 5 V-class Li metal batteries, including electrolyte additives, [10, 11] sulfone-based [12] and fluorinated solvent-based electrolytes, [13, 14] and solid-state electrolytes. [15, 16] Salt-concentrated electrolytes are promising electrolyte systems for 5 V-class Li metal batteries. [17-19] In these electrolytes, most solvent molecules and anions are coordinated with Li^+, forming a peculiar solution structure that differs from conventional dilute electrolytes with many free solvent molecules and anions. The coordination of anions to Li^+ enhances the reduction potential of the anion, resulting in the formation of an SEI from the reductive decomposition products of the anion. [20, 21] For instance, lithium bis(fluorosulfonyl)amide (LiFSA)-concentrated electrolytes

form an FSA-derived SEI on Li metal and improve the CE of Li plating/stripping reactions. [18, 22-26] Additionally, the solution structure suppresses transition metal dissolution from the cathodes and improves the oxidation stability of the electrolytes by increasing the oxidation potential of the solvent molecules and anions. [25, 27-30] Therefore, LiFSA-concentrated electrolytes can improve the cycling performance of 5 V-class Li metal batteries,[17, 18] but further improvements in the CE of Li metal anodes and the cycling stability of 5 V-class cathodes are required for practical use.

In this study, we aimed to improve the performance of 5 V-class Li metal batteries by the gelation of salt-concentrated electrolytes. Introducing polymers with gelation and low solvation ability to concentrated electrolytes would form gel polymer electrolytes with similar local coordination environments of Li^+ as the original concentrated electrolytes. The obtained gel electrolytes are expected to exhibit not only the same functions as the original concentrated electrolytes but also new functions unique to polymer gels. For example, compared with a liquid electrolyte-soaked polymer separator with a non-uniform surface pore structure, a flexible polymer gel with a smooth surface may provide uniform Li^+ flux and pressure distribution on the electrode, which should suppress Li whisker growth and promote dense Li deposition. Additionally, a polymer matrix with low solvation ability may suppress the dissolution of transition metals from the cathode and their deposition on the anode. Furthermore, gel electrolytes prevent leakage of the electrolyte solution, thereby improving battery safety. [31]

Although the operation of a 5 V-class Li metal battery with a gel polymer electrolyte containing a concentrated electrolyte has been demonstrated, [16] the benefits of gelation of concentrated electrolytes with weakly coordinating polymers for Li metal anodes and 5 V-class cathodes are unknown.

Herein, we report a salt-concentrated gel polymer electrolyte containing a LiFSA-concentrated sulfolane (SL) solution and poly(vinylidene fluoride-*co*-hexafluoropropylene) (PVDF-HFP), which improves the performance of 5 V-class Li metal batteries. For the salt, we selected LiFSA, which has high solubility and good SEI-forming ability for Li metal anodes. [22-26] SL was used as the solvent because of its high oxidation stability and superior Li^+ transport properties in salt-concentrated electrolytes. [32, 33] As a polymer, we adopted PVDF-HFP with gelation and low solvation ability to maintain the local Li^+ coordination environments of the original concentrated electrolyte. [34] The salt-concentrated gel electrolyte achieves dense deposition morphology and a high CE of Li metal anodes, along with sufficient oxidation stability against 5 V-class cathodes. Furthermore, the gel electrolyte enables stable cycling of a 5 V-class Li metal battery with a thin Li metal anode (20 μm thickness) and a practical loading $LiNi_{0.5}Mn_{1.5}O_4$ cathode (2.2 mAh cm^{-2}) by inhibiting the deposition of transition metals dissolved from the cathode onto the anode.

2. EXPERIMENTAL SECTION

2.1. Materials.

Battery-grade SL and dimethyl carbonate (DMC) were purchased from Kishida Chemical. LiFSA and PVDF-HFP (Kynar Flex 2801-00) were provided by Nippon Shokubai and Arkema, respectively. 1.0 M $LiPF_6$/ethylene carbonate (EC):ethyl methyl carbonate (EMC) (3:7 v/v) electrolyte was purchased from MU Ionic Solutions. All the reagents were used as received. A concentrated LiFSA/3SL electrolyte (LiFSA:SL molar ratio of 1:3) was prepared by dissolving a specific amount of LiFSA in SL in an Ar-filled glove box (Miwa Manufacturing, H_2O and O_2 levels below 1 ppm).

A concentrated LiFSA/3SL:PVDF-HFP gel electrolyte was prepared using the solution casting method. [35] First, the concentrated LiFSA/3SL electrolyte and PVDF-HFP were dissolved in dehydrated acetone (99.5%, FUJIFILM Wako Pure Chemical) at a weight ratio of LiFSA/3SL electrolyte:PVDF-HFP = 7:3. The casting solution was then poured into a glass Petri dish, and left to evaporate acetone in a dry room (dew point below −50 °C). Subsequently, the obtained gel membrane was dried under vacuum at 25 °C overnight and then punched into a circular shape. The thickness of the gel electrolyte membranes was approximately 150 μm. A composite consisting of the gel electrolyte and a polypropylene (PP) separator was prepared by a similar procedure. The casting solution was poured over a PP separator in a glass Petri dish, and the acetone was allowed to evaporate. The obtained composite membrane was dried under vacuum. The thickness of the composite membrane was approximately 50 μm, and the

membrane thicknesses were controlled by varying the volume of the casting solution.

$LiNi_{0.5}Mn_{1.5}O_4$ powder (Nippon Chemical Industrial), acetylene black (HS-100, Denka), and poly(vinylidene fluoride) (PVDF, L#9130, Kureha) were combined in a weight ratio of 90:5:5 using *N*-methyl-2-pyrrolidone (Kishida Chemical). The resulting slurry was applied onto an Al foil (20 μm thickness) using a doctor blade and then dried at 80 °C for 60 min in an air oven. Subsequently, the dried sheet was pressed and dried overnight at 120 °C under vacuum. Finally, the obtained sheet was punched to create disk electrodes (14 mm diameter) with an active material mass loading of approximately 15 mg cm^{-2} and a cathode areal capacity of 2.2 mAh cm^{-2}. Cu foil (18 μm thickness) and 2032-type coin cell parts (stainless steel cathode case, Al-coated stainless steel cathode case, stainless steel anode case, stainless steel spring, stainless steel spacer, and PP gasket) were purchased from Hoshen. Li foil (600 μm thickness and 200 μm thickness) and Li/Cu foil (20/10 μm thickness) were obtained from Honjo Metal.

2.2. Electrochemical Measurements.

The oxidation stability of the electrolytes was evaluated by linear sweep voltammetry (LSV) using an electrochemical measurement system (HZ-Pro S12, Hokuto Denko) at a scan rate of 1 mV s^{-1} at approximately 25 °C. For the liquid electrolytes, a three-electrode cell (VB7, EC Frontier) with a platinum disk (1.6 mm diameter) as the working electrode and Li metal as

the reference and counter electrodes was used. For the gel electrolyte, a two-electrode cell (SB2A, EC Frontier) with a platinum disk (10 mm diameter) as the working electrode and Li metal as the counter electrode was used.

Li/Cu and Li/Li symmetric cells were assembled as 2032-type coin cells in the glove box. For the electrolytes, 1.0 M $LiPF_6$/EC:EMC, concentrated LiFSA/3SL, and LiFSA/3SL:PVDF-HFP gel electrolytes were used. The volume of 1.0 M $LiPF_6$/EC:EMC and the concentrated LiFSA/3SL electrolytes was 80 μL. A PP separator was used for the 1.0 M $LiPF_6$/EC:EMC electrolyte, and a surfactant-coated PP separator was used for the concentrated LiFSA/3SL electrolyte owing to its poor wettability on the PP separator. The thickness of the Li disk electrodes (12 mm diameter) was 600 μm for the Li/Cu cells and 200 μm for the Li/Li symmetric cells.

Li plating and stripping tests were conducted in the Li/Cu cells using a charge/discharge test system (TOSCAT-3100, Toyo System) at a current density of 0.5 mA cm^{-2} at 25 °C. The effective area for Li plating/stripping was 1.13 cm^2 (12 mm diameter). Li metal was deposited on the Cu foil for 2 h (a plating capacity of 1.0 mAh cm^{-2}) and then stripped until the voltage reached 1.0 V during each cycle. CE was calculated by dividing the stripping capacity by the plating capacity. The average CE was calculated from the 2nd to 20th cycles.

Li^+ dynamics at the interface between Li metal and the electrolytes were studied by electrochemical impedance spectroscopy (EIS, VMP-300 potentiostat, BioLogic) using the

Li/Li symmetric cells in a 1 MHz–0.01 Hz frequency range with an applied AC voltage amplitude of ±5 mV at 25–45 °C. The measurements were performed after 1 cycle of Li plating/stripping at a current density of 0.5 mA cm^{-2} and a plating capacity of 1.0 mAh cm^{-2} at 25 °C. To identify the SEI resistance (R_{SEI}) and charge-transfer resistance (R_{ct}) of the Li metal, EIS was conducted using a three-electrode cell with a Cu disk (16 mm diameter) as the working electrode and Li metal as the reference and counter electrodes at 25 °C. [36] The measurements were carried out at given potentials from open circuit voltage (OCV) to 0.1 V vs. Li/Li^+ and then after Li deposition on the Cu working electrode at a current density of 0.5 mA cm^{-2} and a plating capacity of 0.5 mAh cm^{-2}. The activation energy (E_a) associated with Li^+ transport in the SEI and the interfacial Li^+ transfer of the Li metal was determined from the temperature dependence of R_{SEI} and R_{ct} obtained by EIS.

$Li/LiNi_{0.5}Mn_{1.5}O_4$ full-cells were assembled as 2032-type coin cells in the glove box. An Al-coated stainless steel cathode case was used, and an Al foil (19 mm in diameter) was placed on the cathode case to avoid the corrosion of the stainless steel. Li/Cu foil (20/10 μm thickness) was used as the anode. For the electrolytes, 1.0 M $LiPF_6$/EC:EMC, concentrated LiFSA/3SL, and LiFSA/3SL:PVDF-HFP gel electrolytes were used. The cells with the gel–PP separator composite were assembled in the same way. To prevent internal short circuits in the cells, two PP separators were used for the cells with 1.0 M $LiPF_6$/EC:EMC electrolyte, and two surfactant-coated PP separators were used for the cells with the concentrated LiFSA/3SL

electrolyte. 160 μL of the electrolytes were used for these cells. For the cells with the LiFSA/3SL:PVDF-HFP gel electrolyte and the gel–PP separator composite, 20 μL of the LiFSA/3SL electrolyte was added between the $LiNi_{0.5}Mn_{1.5}O_4$ electrode and the gel to fully wet the porous composite electrode.

Galvanostatic charge/discharge tests of the Li/$LiNi_{0.5}Mn_{1.5}O_4$ full-cells were performed with the charge/discharge test system at a 0.2C rate in a voltage range of 3.5–4.9 V at 25 °C. The 1C rate was 147 mA g^{-1} based on the $LiNi_{0.5}Mn_{1.5}O_4$ weight. The negative to positive capacity ratio of the full-cells was approximately 1.9, corresponding to a Li utilization of 35%.

2.3. Characterization.

The ionic conductivity of the electrolytes was measured by EIS (HZ-7000, Hokuto Denko) in a 200 kHz–1 kHz frequency range with an applied AC voltage amplitude of ±10 mV at 25–60 °C. For the concentrated LiFSA/3SL electrolyte, a four-electrode cell with two outer platinum disk electrodes (10 mm diameter) and two inner platinum wire electrodes (1.0 mm diameter) (SB1400, EC Frontier) was used. For the concentrated LiFSA/3SL:PVDF-HFP gel electrolyte, a two-electrode cell (SB2A, EC Frontier) with two stainless steel-disk electrodes (16 mm diameter) was used.

The electrolyte structures were investigated by Raman spectroscopy with a 785 nm

laser (inVia, Renishaw) at approximately 25 °C. The concentrated LiFSA/3SL and the LiFSA/3SL:PVDF-HFP gel electrolytes were respectively enclosed in a quartz cell in the glove box and a closed chamber with a quartz window (SB1500, EC Frontier) in the dry room to avoid exposure to ambient air.

The surface of the LiFSA/3SL:PVDF-HFP gel electrolyte was observed and analyzed using field emission scanning electron microscopy (FE-SEM, JSM-6700FV, JEOL) and energy-dispersive X-ray spectroscopy (EDS, EX-37001, JEOL). The surface and cross-sectional morphologies of Li deposited on the Cu foil were observed by the FE-SEM. 1.0 mAh cm^{-2} of Li was deposited on the Cu foil using a Li/Cu cell assembled in a split test cell (SB2A, EC Frontier). For the concentrated LiFSA/3SL electrolyte, the Li deposited on the Cu foil was collected from the cell, washed with DMC, and dried in the glove box. For the LiFSA/3SL:PVDF-HFP gel electrolyte, the gel/Li/Cu laminate was collected from the cell and dried under vacuum without washing. The cross-sections of the samples were polished using a cooling cross-section polisher (IB-19520CCP, JEOL) with an ion beam. The transition metals deposited on the Li metal anodes in the Li/$LiNi_{0.5}Mn_{1.5}O_4$ full-cells were analyzed by EDS after 20 charge/discharge cycles. The cycled Li metal anodes were collected from the cells, washed with DMC, and dried in the glove box. All samples were transferred from the glove box to the FE-SEM and cross-section polisher chambers using transfer vessels to avoid exposure to ambient air.

The SEI formed on Li metal was investigated by X-ray photoelectron spectroscopy (XPS, Kratos Ultra 2, Kratos Analytical) with a monochromatic Al Kα X-ray source. The SEI-formed Li disk electrodes were collected from the Li/Cu cells after 10 cycles of Li plating/stripping, washed with DMC, and dried under vacuum. To avoid exposure to air, the obtained samples were moved from the glove box to the XPS chamber using a transfer vessel. The binding energy of the obtained spectra was calibrated against the C 1s peak of amorphous carbon at 285.0 eV. The spectra were fitted using a pseudo-Voigt function (i.e., a linear combination of Gaussian and Lorentzian functions) after Shirley-type background subtraction.

2.4. Computational Methods.

Density functional theory-based molecular dynamics (DFT-MD) simulations of the electrolytes were performed using the CP2K code, [37] which is a first-principles calculation code based on DFT, using the DZVP-MOLOPT-SR-GTH type mixed Gaussian and plane wave basis sets. The cut-off energy of the plane wave was 400 Ry. The PBE functional [38] with a D3 type semi-empirical van der Waals correction [39] and GTH norm-conserving pseudopotentials [40] were used. The DFT-MD simulations with the *NVT* ensemble and a time step of 1 fs were performed using a Nosé-Hoover chain thermostat [41-43] with a chain length of three.

An oligomer consisting of seven VDF and one HFP molecules was selected as a model of PVDF-HFP for the simulations of the concentrated LiFSA/3SL:PVDF-HFP gel electrolyte.

In the oligomer, three VDF, one HFP, and four VDF molecules were polymerized in that order by the formation of C–C bonds. Both ends of the oligomer were terminated with H atoms. The initial atomic structures of the molecules were optimized using Gaussian16 code with B3LYP/cc-pVDZ. In the simulations, three oligomer molecules and LiFSA/3SL liquid consisting of seven Li^+, seven FSA^-, and 21 SL molecules were introduced in a cubic cell using the packmol code. [44] The mass ratio of the LiFSA/3SL liquid to the oligomer was 2.18, which was close to the experimental value (2.33). For reference, the DFT-MD simulations of the concentrated LiFSA/3SL electrolyte which consists of 10 Li^+, 10 FSA^-, and 30 SL molecules were also performed. The parameters of the cubic cells were determined based on the experimental density of the electrolytes. Details of the electrolyte models are summarized in Table S1. First, the DFT-MD simulations were performed at 450 K for 100 ps to optimize the initial atomic structures, followed by the simulations at 300 K for 100 ps. The atomic structures of the last 50 ps were used to calculate the radial distribution functions from Li^+. The coordination number of each atom with Li^+ was obtained by integrating the radial distribution functions.

3. RESULTS AND DISCUSSION

3.1. Electrolyte Structures and Oxidation Stability.

Figure S1 shows the photographs and ionic conductivity of the concentrated LiFSA/3SL electrolyte (LiFSA:SL molar ratio of 1:3) and concentrated LiFSA/3SL:PVDF-HFP gel electrolyte (LiFSA/3SL electrolyte:PVDF-HFP weight ratio of 7:3). The gel membranes were self-standing, flexible, and exhibited no electrolyte solution leakage (Figure S1b). The coordination environments of Li^+ in the electrolytes were investigated using Raman spectroscopy. Figure 1a shows the Raman spectra within the regions corresponding to the SO_2 scissoring mode of SL. A broadened peak was observed for the concentrated LiFSA/3SL electrolyte because the SL molecules solvated Li^+ as monodentate and bridging ligands. [33] The Raman spectra within the regions of the S–N stretching mode of FSA^- are shown in Figure 1b. The spectrum of the concentrated LiFSA/3SL electrolyte showed that FSA^- and Li^+ formed contact ion pairs (CIPs, ~732 cm^{-1}) and aggregates (AGGs, higher than 745 cm^{-1}). [28] The concentrated LiFSA/3SL:PVDF-HFP gel electrolyte showed a similar spectrum to that of the concentrated LiFSA/3SL electrolyte, indicating that PVDF-HFP with low solvation ability hardly coordinates Li^+, and thus the local coordination environments of SL–Li^+–FSA^- were maintained in the PVDF-HFP matrix of the gel electrolyte. [34]

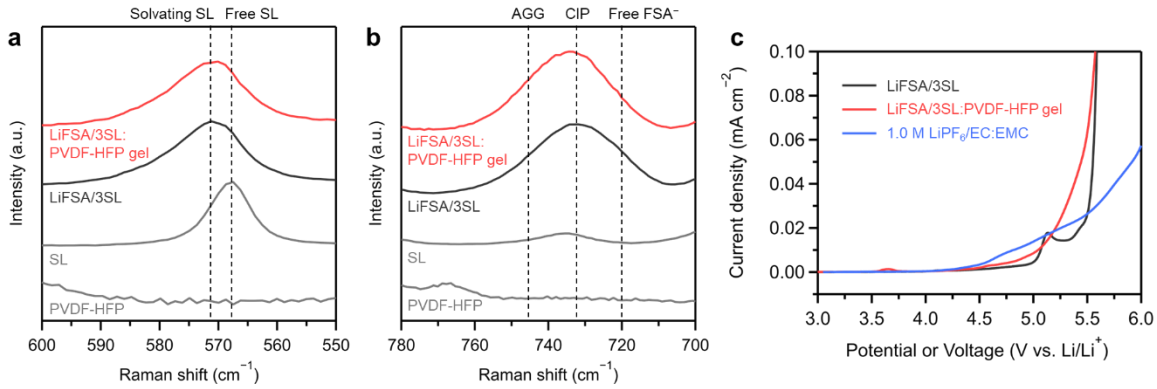

Figure 1. (a,b) Raman spectra of the LiFSA/3SL and LiFSA/3SL:PVDF-HFP gel electrolytes within the regions of the (a) SO_2 scissoring mode of SL and (b) S–N stretching mode of FSA^-. (c) Oxidation stability of LiFSA/3SL, LiFSA/3SL:PVDF-HFP gel, and 1.0 M $LiPF_6$/EC:EMC electrolytes on Pt. LSV was performed at a scan rate of 1 mV s^{-1} at approximately 25 °C. A three-electrode cell with Pt as the working electrode and Li metal as the reference and counter electrodes was used for the liquid electrolytes. A two-electrode cell with Pt as the working electrode and Li metal as the counter electrode was used for the gel electrolyte.

DFT-MD simulations of the electrolytes were performed to support the Raman spectroscopic analysis. To simulate the concentrated LiFSA/3SL:PVDF-HFP gel electrolyte, an oligomer polymerized with three VDF, one HFP, and four VDF molecules in that order was used as a model of PVDF-HFP. Snapshots of representative electrolyte structures are shown in Figure 2a,d. Li^+ is coordinated by O atoms of SL and FSA^- in both electrolytes. To quantitatively analyze the coordination environments of Li^+ in the electrolytes, we calculated the radial distribution functions, $g(r)$, from Li^+ (Figure 2b,e) and the coordination numbers, $N(r)$,

of each atom to Li^+ (Figure 2c,f). Sharp peaks of Li^+–O (SL) and Li^+–O (FSA^-) were observed at around 2 Å in both electrolytes, whereas F atoms of PVDF-HFP oligomer model were almost absent in this region for the gel electrolyte (Figure 2b,e). This indicates that Li^+ is dominantly coordinated by O atoms of SL and FSA^- rather than F atoms of PVDF-HFP and that the solvation ability of PVDF-HFP is very weak. In both electrolytes, Li^+ is coordinated by approximately three O atoms of SL and one O atom of FSA^- (Figure 2c,f), supporting that the local coordination environments of Li^+ are maintained after the introduction of PVDF-HFP into the concentrated LiFSA/3SL electrolyte.

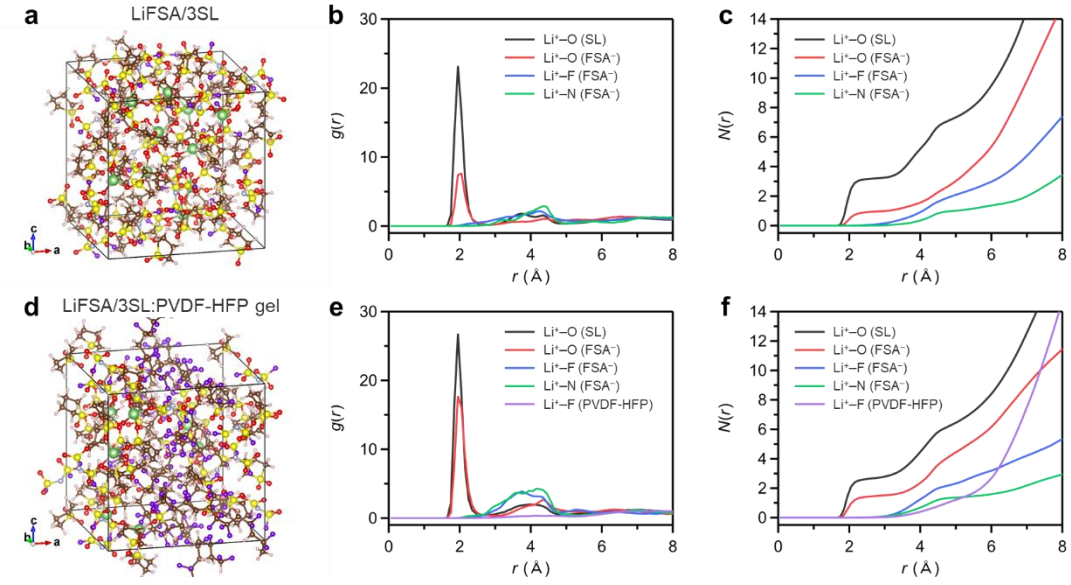

Figure 2. DFT-MD simulations of the (a–c) LiFSA/3SL and (d–f) LiFSA/3SL:PVDF-HFP gel electrolytes. (a,d) Snapshots of the representative equilibrium trajectories: H, light pink; Li, green; C, brown; O, red; N, light gray; S, yellow; and F, purple. (b,e) Radial distribution

functions, $g(r)$, and (c,f) coordination numbers, $N(r)$, as functions of distances between Li^+ and N, O, and F atoms in SL, FSA^-, and the oligomer as a model of PVDF-HFP.

The oxidation stability of the electrolytes on platinum was evaluated by LSV (Figure 1c). The concentrated LiFSA/3SL electrolyte showed high oxidation stability above 5 V vs. Li/Li^+, which is higher than that of the conventional 1.0 M $LiPF_6$/EC:EMC electrolyte. This is attributed to the intrinsic high oxidation stability of SL molecule [32] as well as the coordination of the SL and FSA^- to Li^+ in the LiFSA/3SL electrolyte. This coordination environment induces partial electron donation from the SL molecule and FSA^- to Li^+, enhancing the oxidation potential of the solvent molecule and anion. [27, 29] The concentrated LiFSA/3SL:PVDF-HFP gel electrolyte also showed high oxidation stability approaching 5 V vs. Li/Li^+, which was sufficiently stable for the charge/discharge reaction potential of $LiNi_{0.5}Mn_{1.5}O_4$.

3.2. Li Plating/Stripping Efficiency and Li Deposition Morphology.

We evaluated the CE of the Li plating and stripping reactions in the electrolytes using Li/Cu cells (Figure 3a–c). In the concentrated LiFSA/3SL electrolyte, the CE was 71.4% in the 1st cycle and gradually reached approximately 98% over 10 cycles (Figure 3a,c). In the concentrated LiFSA/3SL:PVDF-HFP gel electrolyte, the CE was 83.9% in the 1st cycle, reached over 98% within four cycles, and maintained stable cycling for more than 50 cycles

(Figure 3b,c). The LiFSA/3SL:PVDF-HFP gel electrolyte showed higher CE than the LiFSA/3SL electrolyte during cycling, resulting in a higher average CE from the 2nd to the 20th cycle of 98.5% (the average CE of the LiFSA/3SL electrolyte was 96.9%). These results indicate that the gelation of the concentrated electrolyte with PVDF-HFP enhances the Li plating and stripping performance.

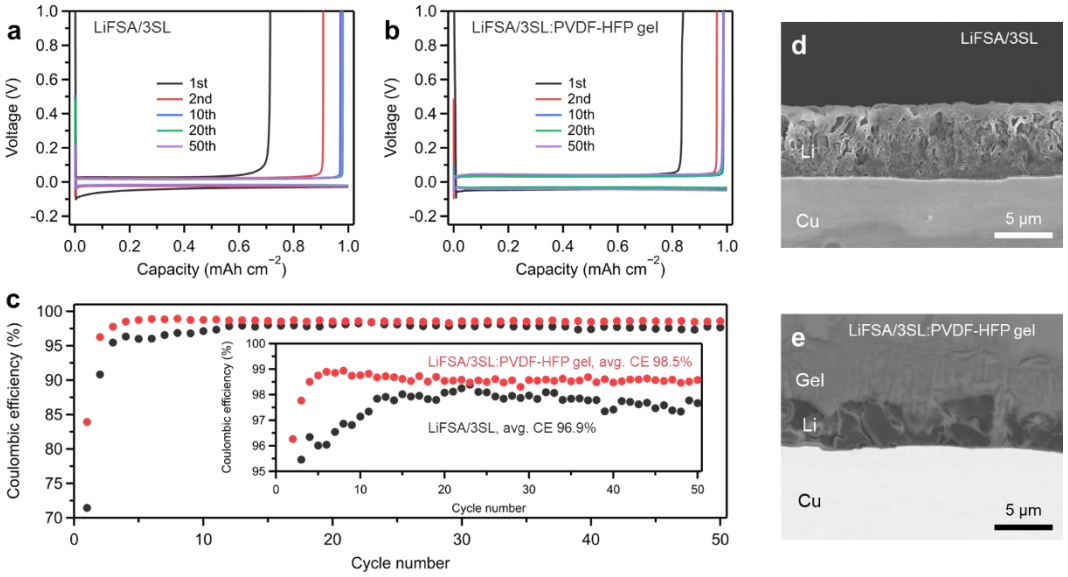

Figure 3. (a,b) Li plating/stripping curves in the (a) LiFSA/3SL and (b) LiFSA/3SL:PVDF-HFP gel electrolytes using Li/Cu cells at a current density of 0.5 mA cm^{-2} and a plating capacity of 1.0 mAh cm^{-2}. (c) CE of Li plating/stripping reactions for the electrolytes during cycling. The inset is a magnified view. The average CE was calculated from the 2nd to the 20th cycle. (d,e) Cross-sectional morphology of Li deposited on Cu foils in the electrolytes at a current density of 0.5 mA cm^{-2} and a plating capacity of 1.0 mAh cm^{-2}. (d) A secondary electron image

of the Li deposited in LiFSA/3SL electrolyte. (e) A backscattered electron image of the Li deposited in LiFSA/3SL:PVDF-HFP gel electrolyte.

The morphology of the Li metal deposited in the electrolytes was observed by the FE-SEM. The Li metal deposited in the concentrated LiFSA/3SL electrolyte was granular, as shown in the surface image (Figure S2); however, the cross-sectional morphology was porous and contained Li whiskers (Figure 3d). In the LiFSA/3SL:PVDF-HFP gel electrolyte, larger granular Li metal was densely deposited, as shown in the cross-sectional image in Figure 3e. The large and dense deposition morphology reduces the surface area of the Li metal anode, limiting the reductive decomposition of the electrolytes. In addition, the granular morphology should suppress the formation of inactive Li during the Li dissolution process. [4] Thus, the gel electrolyte achieved a higher CE of the Li plating/stripping reactions. The dense Li deposition morphology and enhanced CE must be due to the low-resistance SEI described later and the unique properties of the gel electrolyte. Compared with the liquid electrolyte-soaked PP separator with a non-uniform surface pore structure, the gel electrolyte has a smooth surface and homogeneous composition (Figure S3), which may provide uniform Li^+ flux and pressure distribution on the electrode surface, suppress whisker-like Li growth, and promote dense Li deposition.

3.3. Li^+ Dynamics at Li/Electrolyte Interface.

The Li^+ dynamics at the Li/electrolyte interface significantly affect the Li deposition morphology and CE of the Li plating/stripping reactions. We studied the Li^+ dynamics at the interface using EIS with Li/Li symmetric cells. Figure 4a shows the Nyquist plots of the Li/Li symmetric cells using different electrolytes after one cycle of Li plating/stripping. Both spectra consist of two semicircles in the frequency ranges of approximately 100 kHz–100 Hz and 100–0.1 Hz along with a sloping line. The intersection of the semicircle with the real axis and the sloping line are assigned to the bulk electrolyte resistance (R_{bulk}) and the Warburg impedance (Z_W) related to the diffusion of Li^+, respectively. To identify which semicircles correspond to the SEI resistance (R_{SEI}) and charge-transfer resistance (R_{ct}) of the Li metal, EIS was conducted using a three-electrode cell equipped with a Cu working electrode and Li metal reference and counter electrodes. [36] Figure 4b,c shows the variation in the Nyquist plots of the cell using the concentrated LiFSA/3SL electrolyte at given potentials from OCV to 0.1 V vs. Li/Li^+ and then after Li deposition on the working electrode. At 1.0 and 0.1 V vs. Li/Li^+, one semicircle was observed in the 100 kHz–100 Hz frequency range, which is attributed to the formation of a SEI on the working electrode. After Li deposition on the working electrode, another semicircle appeared in the 100–0.1 Hz frequency range, indicating that the semicircle is assigned to the R_{ct} of the deposited Li metal. A similar result was obtained for the cell using the LiFSA/3SL:PVDF-HFP gel electrolyte (Figure S4). Therefore, the two semicircles in the 100

kHz–100 Hz and 100–0.1 Hz frequency ranges correspond to the R_{SEI} and R_{ct} of the Li metal, respectively.

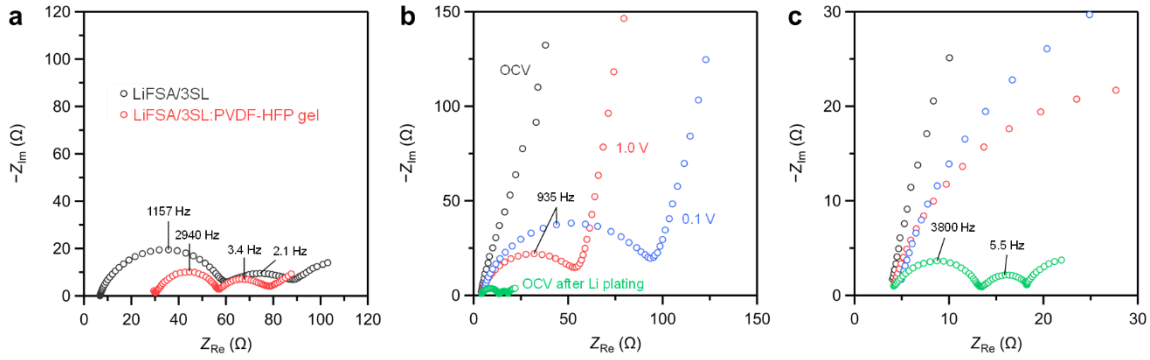

Figure 4. (a) Nyquist plots of EIS for Li/Li symmetric cells using the LiFSA/3SL and LiFSA/3SL:PVDF-HFP gel electrolytes at 25 °C after one cycle of Li plating/stripping. Li disks with 12 mm diameter were used. (b) Nyquist plots of EIS for a three-electrode cell with a Cu disk (16 mm diameter) as a working electrode and Li metal as reference and counter electrodes using LiFSA/3SL electrolyte at 25 °C. The measurements were carried out at given potentials from OCV to 0.1 V vs. Li/Li^+ and then after Li plating on the working electrode. (c) Magnified views of (b).

To obtain the R_{SEI} and R_{ct} of the Li metal, the Nyquist plots of the Li/Li symmetric cells (Figure 4a) were fitted using an equivalent circuit model (Figure S5). The R_{SEI} and R_{ct} values were calculated as single-sided resistances because the symmetric cells were measured. Table S2 lists the resistance values obtained. The R_{SEI} of the LiFSA/3SL:PVDF-HFP gel

electrolyte was much lower than that of the concentrated LiFSA/3SL electrolyte, suggesting that a highly Li^+-conductive SEI was formed by the gel electrolyte. Facile Li^+ transport in the SEI should contribute to the dense Li deposition because sluggish Li^+ transport on the deposited Li surface has been reported to cause the deposition of Li whiskers. [45] We analyzed the temperature dependence of the R_{SEI} and R_{ct} of the Li metal (Figure S6), and the values from the EIS measurements are shown in Figure S7. The activation energies (E_a) for Li^+ transport in the SEI and interfacial Li^+ transfer of the Li metal were evaluated using the Arrhenius equation. The E_a for Li^+ transport in the SEI (45–47 kJ mol^{-1}) was almost comparable to that for the interfacial Li^+ transfer of Li metal (41 kJ mol^{-1}), suggesting that both processes dominate the kinetics of the Li plating/stripping reactions.

3.3. SEI Chemistry.

Furthermore, we studied the SEI on Li metal by XPS owing to the important role of SEI in improving Li metal anodes and Li^+ dynamics at the Li/electrolyte interface. Figure 5 shows the composition of the SEI formed in the concentrated LiFSA/3SL and LiFSA/3SL:PVDF-HFP gel electrolytes. In the LiFSA/3SL electrolyte, the SEI had a high C concentration owing to the decomposition of SL. [24] The SEI formed in the LiFSA/3SL:PVDF-HFP gel electrolyte had higher F and S concentrations and lower C concentration than the SEI formed in the LiFSA/3SL electrolyte, indicating that the gelation with PVDF-HFP promoted

the formation of an SEI rich in fluorine and sulfur compounds.

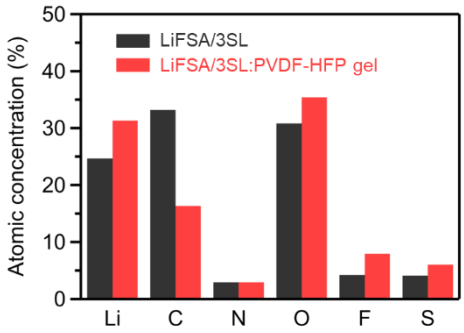

Figure 5. Composition of the SEI formed on Li metal using the LiFSA/3SL and LiFSA/3SL:PVDF-HFP gel electrolytes. The values were obtained using the XPS spectra.

The chemical state of the constituent elements of the SEI was analyzed from high-resolution XPS spectra (Figures 6 and S8). In the C 1s spectra, the intensities of the C–C/C–H and C–S peaks were lower in the SEI formed in the LiFSA/3SL:PVDF–HFP gel electrolyte, suggesting suppressed SL decomposition. [18, 24] The F 1s and S 2p spectra reveal that the SEI formed by the gel electrolyte contained more lithium fluoride (LiF) and sulfur compounds. [18, 20, 24] LiF should be formed via the interfacial reaction between PVDF-HFP and Li metal. [46, 47] Additionally, as confirmed by Raman spectroscopy (Figure 2a,b) and DFT-MD simulations (Figure 3), the gel electrolyte had the solvation structures of SL–Li^+–FSA^- similar to those in the original LiFSA/3SL electrolyte. Studies have shown that the Li^+–FSA^- coordination raises the reduction potential of FSA^-, leading to the sacrificial reduction of FSA^- and the formation

of FSA-derived SEI rich in LiF and sulfur compounds. [18, 20, 21] FSA-derived components and LiF have been reported to offer low resistance and high stability at the Li/electrolyte interface, improving the CE of the Li plating/stripping reactions and Li deposition morphology. [19, 24, 26] Thus, we expect that the F- and S-rich SEI formed by the gel electrolyte will provide high ionic conductivity and stability, achieving the enhanced CE of the Li plating/stripping reactions and the dense Li deposition morphology.

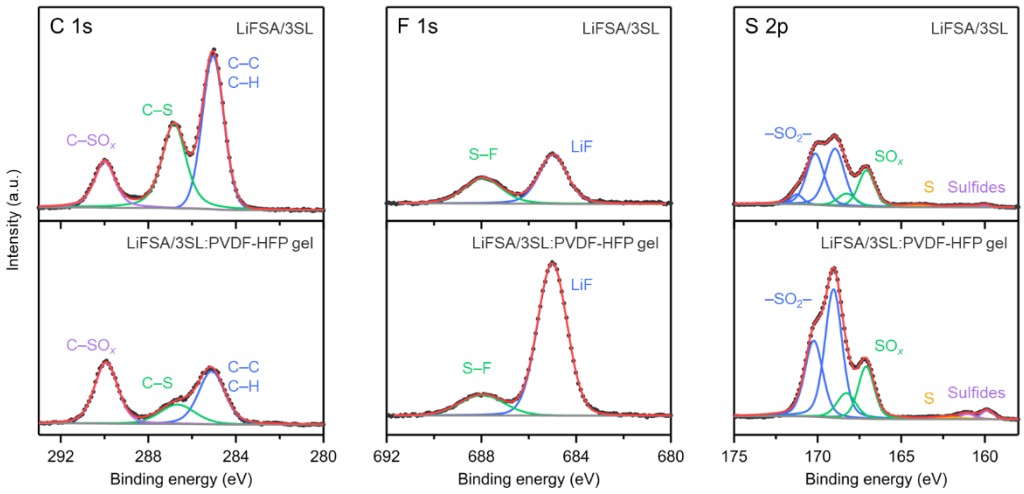

Figure 6. C 1s, F 1s, and S 2p XPS spectra of the SEI formed on Li metal using the LiFSA/3SL and LiFSA/3SL:PVDF-HFP gel electrolytes.

3.4. Charge/Discharge Performance of High-Voltage Li Metal Batteries.

To evaluate the applicability of the LiFSA/3SL:PVDF-HFP gel electrolyte to high-voltage Li metal batteries, we conducted charge/discharge tests of the full-cells combining a thin Li meta anode (20 μm thickness) and a 5 V-class $LiNi_{0.5}Mn_{1.5}O_4$ cathode (2.2 mAh cm^{-2})

with a charge cut-off voltage at 4.9 V (Figure 7a–d). The negative to positive capacity ratio of the Li/$LiNi_{0.5}Mn_{1.5}O_4$ full-cells was approximately 1.9 (~35% Li utilization), which is a severe condition among previously reported cells. [10, 11, 13-18, 48] The cell with the conventional 1.0 M $LiPF_6$/EC:EMC electrolyte was stable for approximately five cycles, but the capacity suddenly faded (Figure 7c,d). This degradation is due to the low CE and poor cycling stability of the Li plating/stripping reactions in the electrolyte, which quickens the depletion of Li during cycling (Figure S9). For the concentrated LiFSA/3SL electrolyte, the capacity gradually decreased and the CE fluctuated during cycling (Figure 7a,d), despite the electrolyte showing a higher CE of Li metal anodes and higher oxidation stability than the conventional 1.0 M $LiPF_6$/EC:EMC electrolyte. As observed in Figures 7a and S10, voltage fluctuations often occurred from the 20th charging process, resulting in a significant drop in the CE of the charge/discharge reactions. This behavior can be attributed to micro-short circuits caused by Li whisker growth during the charging process. [49, 50] The cell using the LiFSA/3SL:PVDF-HFP gel electrolyte–PP separator composite showed significantly improved cycling performance with 99.5% capacity retention after 50 cycles and an average CE of 99.4% (Figure 7b,d), in contrast to the concentrated LiFSA/3SL electrolyte (41.0% capacity retention after 50 cycles and an average CE of 89.6%) and the 1.0 M $LiPF_6$/EC:EMC electrolyte (13.4% capacity retention after 10 cycles and an average CE of 82.1%). The cell using the LiFSA/3SL:PVDF-HFP gel electrolyte also showed stable charge/discharge behavior but suffered a short circuit on the 22nd charging process

(Figure S11), which was probably caused by Li deposition in the gel electrolyte that reached the cathode. These results demonstrate that the gel electrolyte–PP separator composite effectively prevents internal short circuits of the cells and stabilizes the charge/discharge cycling.

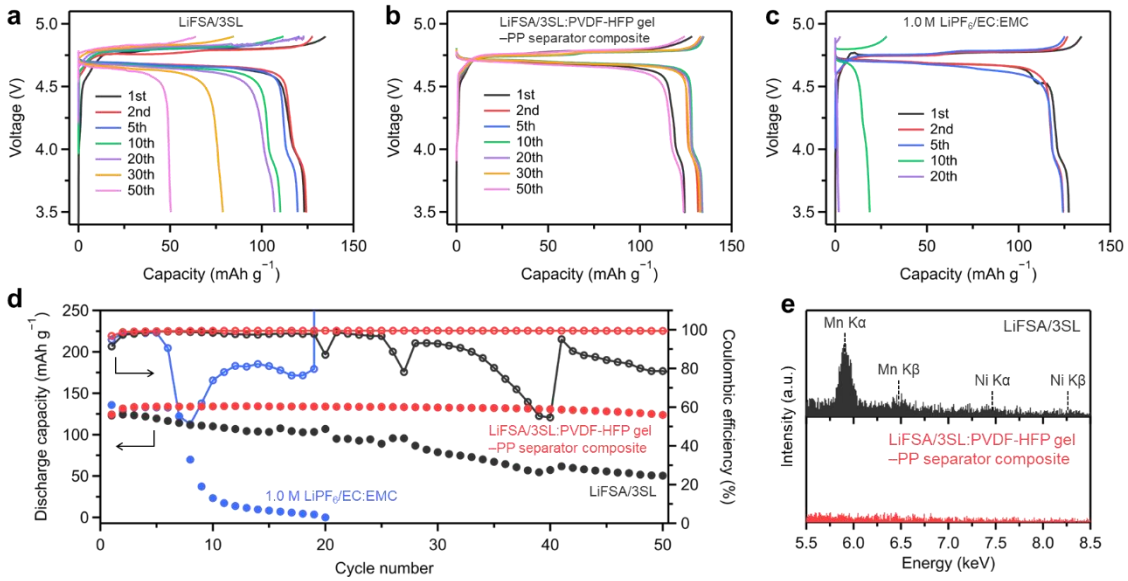

Figure 7. (a–c) Charge/discharge curves of Li/$LiNi_{0.5}Mn_{1.5}O_4$ full-cells using the (a) LiFSA/3SL electrolyte, (b) LiFSA/3SL:PVDF-HFP gel electrolyte–PP separator composite, and (c) 1.0 M $LiPF_6$/EC:EMC electrolyte. (d) Discharge capacity and CE vs. cycle number of the cells. The tests were performed at a 0.2C rate in a voltage range of 3.5–4.9 V. (e) EDS spectra of the cycled Li metal anodes in the cells using the LiFSA/3SL electrolyte and LiFSA/3SL:PVDF-HFP gel electrolyte–PP separator composite after 20 charge/discharge cycles.

The deposition of transition metals dissolved from the cathode onto the anode

reportedly induces the growth of Li whiskers and results in micro short circuits of the cell. [50] The EDS analysis indicated a high content of Mn and Ni on the cycled Li metal anode in the cell using the concentrated LiFSA/3SL electrolyte (Figure 7e). The transition metals deposited on the Li metal anode should promote Li whisker growth and cause micro short circuits, leading to the voltage fluctuations during the charging process and the poor cycling performance (Figures 7a,d and S10). In contrast, almost no Mn or Ni was detected on the cycled Li metal anode with the LiFSA/3SL:PVDF-HFP gel electrolyte–PP separator composite (Figure 7e). This is probably due to the polymer network of PVDF-HFP with a low solvation ability, which prevents the dissolution, diffusion, and migration of the transition metal ions from the cathode to the anode. [25] Therefore, the superior cycling performance of the high-voltage Li metal battery using the gel electrolyte–PP separator composite is attributed to the high CE and dense deposition morphology of the Li metal anode (Figure 3c,e), the high oxidation stability (Figure 1c), and the prevention of transition metal deposition on the anode (Figure 7e).

4. CONCLUSIONS

We investigated the gelation of a salt-concentrated electrolyte with weakly coordinating PVDF-HFP to improve the performance of high-voltage Li metal batteries. The concentrated LiFSA/3SL:PVDF-HFP gel electrolyte simultaneously provides a high CE of the Li plating/stripping reactions, a dense deposition morphology of Li metal, high oxidation

stability, and the ability to inhibit the deposition of transition metals dissolved from the cathode onto the anode. For the gel electrolyte, the solvation structures of SL–Li^+–FSA^- similar to those in the original concentrated LiFSA/3SL electrolyte are maintained in the PVDF-HFP matrix, which leads to the formation of the low-resistance SEI rich in LiF and sulfur compounds. The above features of the gel electrolyte stabilize the charge/discharge cycling of a 5 V-class Li metal battery with a thin Li metal anode (20 μm thickness) and a practical loading $LiNi_{0.5}Mn_{1.5}O_4$ cathode (2.2 mAh cm^{-2}). Although our electrolyte and interface design strategy will contribute to the development of high-voltage Li metal batteries, challenges remain for the practical application. Our future work will involve the optimization and development of electrolyte formulations and composites of salt-concentrated gel electrolytes and functional separators, [24, 51] which should further enhance the performance of high-voltage Li metal batteries. Furthermore, the flexible and self-standing gel electrolyte is a promising interlayer for forming good contact between solid materials in solid-state batteries. We plan to utilize the gel electrolyte as an interlayer between solid electrolytes and Li metal anodes to stabilize the Li plating/stripping reactions.

ASSOCIATED CONTENT

Supporting Information

The Supporting Information is available free of charge at

Photographs and ionic conductivity of the electrolytes, electrolyte models used in DFT-MD simulations, surface SEM images of electrodeposited Li, surface SEM images and elemental maps of LiFSA/3SL:PVDF-HFP gel electrolyte, Nyquist plots of EIS and an equivalent circuit model used for fitting, values and temperature dependence of R_{SEI} and R_{ct}, XPS spectra of SEI, Li plating/stripping stability in Li/Cu cells using 1.0 M $LiPF_6$/EC:EMC electrolyte, and charge/discharge performance of Li/$LiNi_{0.5}Mn_{1.5}O_4$ full-cells using LiFSA/3SL and LiFSA/3SL:PVDF-HFP gel electrolytes

AUTHOR INFORMATION

Corresponding Author

Yuta Maeyoshi – Research Institute of Electrochemical Energy, Department of Energy and Environment, National Institute of Advanced Industrial Science and Technology (AIST), 1-8-31 Midorigaoka, Ikeda, Osaka 563-8577, Japan; https://orcid.org/0000-0002-4612-8283; Email: y.maeyoshi@aist.go.jp

Authors

Kazuki Yoshii – Research Institute of Electrochemical Energy, Department of Energy and Environment, National Institute of Advanced Industrial Science and Technology (AIST), 1-8-31 Midorigaoka, Ikeda, Osaka 563-8577, Japan; https://orcid.org/0000-0001-8904-6790

Hikaru Sano – Research Institute of Electrochemical Energy, Department of Energy and Environment, National Institute of Advanced Industrial Science and Technology (AIST), 1-8-31 Midorigaoka, Ikeda, Osaka 563-8577, Japan; https://orcid.org/0000-0002-7557-0767

Hikari Sakaebe – Research Institute of Electrochemical Energy, Department of Energy and Environment, National Institute of Advanced Industrial Science and Technology (AIST), 1-8-31 Midorigaoka, Ikeda, Osaka 563-8577, Japan; Institute for Materials Chemistry and Engineering, Kyushu University, 6-1 Kasuga koen, Kasuga-shi, Fukuoka 816-8580, Japan; https://orcid.org/0000-0002-2520-1621

Ryota Tamate – Research Center for Macromolecules & Biomaterials, National Institute for Materials Science (NIMS), 1-2-1 Sengen, Tsukuba, Ibaraki 305-0047, Japan; https://orcid.org/0000-0002-1704-1058

Tomoaki Kaneko – Department of Computational Science and Technology, Research Organization for Information Science and Technology (RIST), 1-18-16 Hamamatsucho, Minato-ku, Tokyo 105-0013, Japan; https://orcid.org/0000-0002-5296-7403

Keitaro Sodeyama – Center for Basic Research on Materials, National Institute for Materials Science (NIMS), 1-1 Namiki, Tsukuba, Ibaraki 305-0044, Japan; https://orcid.org/0000-0002-9228-0729

Note

The authors declare no competing financial interest.

ACKNOWLEDGMENTS

This work was partly supported by JSPS KAKENHI (Grant Numbers JP21K14731, JP22H04626, and JP23K13833), Iketani Science and Technology Foundation (Grant Number 0331058-A), and GteX Program Japan (Grant Number JPMJGX23S3). We thank Nippon Shokubai and Arkema for providing lithium bis(fluorosulfonyl)amide (LiFSA) and poly(vinylidene fluoride-*co*-hexafluoropropylene) (PVDF-HFP), respectively.

REFERENCES

1. Tarascon, J.-M.; Armand, M., Issues and challenges facing rechargeable lithium batteries. *Nature* **2001,** *414* (6861), 359-367.
2. Lin, D.; Liu, Y.; Cui, Y., Reviving the lithium metal anode for high-energy batteries. *Nat. Nanotechnol.* **2017,** *12* (3), 194-206.
3. Cheng, X.-B.; Zhang, R.; Zhao, C.-Z.; Wei, F.; Zhang, J.-G.; Zhang, Q., A review of solid electrolyte interphases on lithium metal anode. *Adv. Sci.* **2016,** *3* (3), 1500213.
4. Fang, C.; Li, J.; Zhang, M.; Zhang, Y.; Yang, F.; Lee, J. Z.; Lee, M.-H.; Alvarado, J.; Schroeder, M. A.; Yang, Y.; Lu, B.; Williams, N.; Ceja, M.; Yang, L.;

Cai, M.; Gu, J.; Xu, K.; Wang, X.; Meng, Y. S., Quantifying inactive lithium in lithium metal batteries. *Nature* **2019,** *572* (7770), 511-515.
5. Li, W.; Song, B.; Manthiram, A., High-voltage positive electrode materials for lithium-ion batteries. *Chem. Soc. Rev.* **2017,** *46* (10), 3006-3059.
6. Hu, M.; Pang, X.; Zhou, Z., Recent progress in high-voltage lithium ion batteries. *J. Power Sources* **2013,** *237*, 229-242.
7. Tan, S.; Ji, Y. J.; Zhang, Z. R.; Yang, Y., Recent Progress in Research on High-Voltage Electrolytes for Lithium-Ion Batteries. *ChemPhysChem* **2014,** *15* (10), 1956-1969.
8. Fan, X.; Wang, C., High-voltage liquid electrolytes for Li batteries: progress and perspectives. *Chem. Soc. Rev.* **2021,** *50* (18), 10486-10566.
9. Maeyoshi, Y.; Miyamoto, S.; Noda, Y.; Munakata, H.; Kanamura, K., Effect of organic additives on characteristics of carbon-coated LiCoPO4 synthesized by hydrothermal method. *J. Power Sources* **2017,** *337*, 92-99.
10. Zhou, J.; Hao, B.; Peng, M.; Zhang, L.; Ji, H.; Liu, J.; Ling, W.; Yan, C.; Qian, T., Nonafluorobutane-1-Sulfonic Acid Induced Local High Concentration Additive Interface for Robust SEI Formation of High-Voltage (5 V-Class) Lithium Metal Batteries. *Adv. Energy Mater.* **2023,** *13* (24), 2204174.
11. Yue, H.; Yang, Y.; Xiao, Y.; Dong, Z.; Cheng, S.; Yin, Y.; Ling, C.; Yang, W.; Yu, Y.; Yang, S., Boron additive passivated carbonate electrolytes for stable cycling of 5 V lithium–metal batteries. *J. Mater. Chem. A* **2019,** *7* (2), 594-602.
12. Li, P.; Zhang, H.; Lu, J.; Li, G., Low Concentration Sulfolane-Based Electrolyte for High Voltage Lithium Metal Batteries. *Angew. Chem. Int. Ed.* **2023,** *62* (10), e202216312.
13. Fan, X.; Chen, L.; Borodin, O.; Ji, X.; Chen, J.; Hou, S.; Deng, T.; Zheng, J.; Yang, C.; Liou, S.-C.; Amine, K.; Xu, K.; Wang, C., Non-flammable electrolyte enables Li-metal batteries with aggressive cathode chemistries. *Nat. Nanotechnol.* **2018,** *13* (8), 715-722.
14. Chen, L.; Fan, X.; Hu, E.; Ji, X.; Chen, J.; Hou, S.; Deng, T.; Li, J.; Su, D.; Yang, X.; Wang, C., Achieving High Energy Density through Increasing the Output Voltage: A Highly Reversible 5.3 V Battery. *Chem* **2019,** *5* (4), 896-912.
15. Yu, J.; Hu, Y.; Ma, X.; Zou, X.; Qi, H.; Zhou, Y.; Yan, F., A highly conductive and stable hybrid solid electrolyte for high voltage lithium metal batteries. *J. Mater. Chem. A* **2022,** *10* (24), 12842-12855.
16. Wang, B.; Liu, J.; Ock, J.-y.; Motoyoshi, R.; Li, S.; Ueno, K.; Dokko, K.; Tsuzuki, S.; Watanabe, M., LiNi0.5Mn1.5O4-Hybridized Gel Polymer Cathode and Gel Polymer Electrolyte Containing a Sulfolane-Based Highly Concentrated Electrolyte for the Fabrication of a 5 V Class of Flexible Lithium Batteries. *ACS omega* **2022,** *7* (21), 17732-17740.
17. Suo, L.; Xue, W.; Gobet, M.; Greenbaum, S. G.; Wang, C.; Chen, Y.; Yang, W.; Li, Y.; Li, J., Fluorine-donating electrolytes enable highly reversible 5-V-class Li metal

batteries. *Proc. Natl. Acad. Sci. U.S.A.* **2018,** *115* (6), 1156-1161.
18. Ren, X.; Chen, S.; Lee, H.; Mei, D.; Engelhard, M. H.; Burton, S. D.; Zhao, W.; Zheng, J.; Li, Q.; Ding, M. S.; Schroeder, M.; Alvarado, J.; Xu, K.; Meng, Y. S.; Liu, J.; Zhang, J.-G.; Xu, W., Localized High-Concentration Sulfone Electrolytes for High-Efficiency Lithium-Metal Batteries. *Chem* **2018,** *4* (8), 1877-1892.
19. Yamada, Y.; Wang, J.; Ko, S.; Watanabe, E.; Yamada, A., Advances and issues in developing salt-concentrated battery electrolytes. *Nat. Energy* **2019,** *4* (4), 269-280.
20. Yamada, Y.; Furukawa, K.; Sodeyama, K.; Kikuchi, K.; Yaegashi, M.; Tateyama, Y.; Yamada, A., Unusual stability of acetonitrile-based superconcentrated electrolytes for fast-charging lithium-ion batteries. *J. Am. Chem. Soc.* **2014,** *136* (13), 5039-5046.
21. Sodeyama, K.; Yamada, Y.; Aikawa, K.; Yamada, A.; Tateyama, Y., Sacrificial anion reduction mechanism for electrochemical stability improvement in highly concentrated Li-salt electrolyte. *J. Phys. Chem. C* **2014,** *118* (26), 14091-14097.
22. Qian, J.; Henderson, W. A.; Xu, W.; Bhattacharya, P.; Engelhard, M.; Borodin, O.; Zhang, J.-G., High rate and stable cycling of lithium metal anode. *Nat. Commun.* **2015,** *6*, 6362.
23. Fan, X.; Chen, L.; Ji, X.; Deng, T.; Hou, S.; Chen, J.; Zheng, J.; Wang, F.; Jiang, J.; Xu, K.; Wang, C., Highly Fluorinated Interphases Enable High-Voltage Li-Metal Batteries. *Chem* **2018,** *4* (1), 174-185.
24. Maeyoshi, Y.; Ding, D.; Kubota, M.; Ueda, H.; Abe, K.; Kanamura, K.; Abe, H., Long-Term Stable Lithium Metal Anode in Highly Concentrated Sulfolane-Based Electrolytes with Ultrafine Porous Polyimide Separator. *ACS Appl. Mater. Interfaces* **2019,** *11* (29), 25833-25843.
25. Maeyoshi, Y.; Yoshii, K.; Shikano, M.; Sakaebe, H., Improving Cycling Stability of Vanadium Sulfide (VS4) as a Li Battery Cathode Material Using a Localized High-Concentration Carbonate-Based Electrolyte. *ACS Appl. Energy Mater.* **2021,** *4* (12), 13627-13635.
26. Maeyoshi, Y.; Yoshii, K.; Sakaebe, H., Stable Lithium Metal Plating/Stripping in a Localized High-Concentration Cyclic Carbonate-Based Electrolyte. *Electrochemistry* **2022,** *90* (4), 047001.
27. Yoshida, K.; Nakamura, M.; Kazue, Y.; Tachikawa, N.; Tsuzuki, S.; Seki, S.; Dokko, K.; Watanabe, M., Oxidative-stability enhancement and charge transport mechanism in glyme-lithium salt equimolar complexes. *J. Am. Chem. Soc.* **2011,** *133* (33), 13121-9.
28. Wang, J.; Yamada, Y.; Sodeyama, K.; Chiang, C. H.; Tateyama, Y.; Yamada, A., Superconcentrated electrolytes for a high-voltage lithium-ion battery. *Nat. Commun.* **2016,** *7*, 12032.
29. Ko, S.; Yamada, Y.; Yamada, A., A 4.8 V Reversible Li_2CoPO_4F/Graphite Battery

Enabled by Concentrated Electrolytes and Optimized Cell Design. *Batteries Supercaps* **2020,** *3* (9), 910-916.
30. Ko, S.; Yamada, Y.; Yamada, A., An overlooked issue for high-voltage Li-ion batteries: Suppressing the intercalation of anions into conductive carbon. *Joule* **2021,** *5* (4), 998-1009.
31. Osada, I.; de Vries, H.; Scrosati, B.; Passerini, S., Ionic-Liquid-Based Polymer Electrolytes for Battery Applications. *Angew. Chem. Int. Ed.* **2016,** *55* (2), 500-513.
32. Abouimrane, A.; Belharouak, I.; Amine, K., Sulfone-based electrolytes for high-voltage Li-ion batteries. *Electrochem. Commun.* **2009,** *11* (5), 1073-1076.
33. Dokko, K.; Watanabe, D.; Ugata, Y.; Thomas, M. L.; Tsuzuki, S.; Shinoda, W.; Hashimoto, K.; Ueno, K.; Umebayashi, Y.; Watanabe, M., Direct Evidence for Li Ion Hopping Conduction in Highly Concentrated Sulfolane-Based Liquid Electrolytes. *J. Phys. Chem. B* **2018,** *122* (47), 10736-10745.
34. Kim, C. S.; Oh, S. M., Importance of donor number in determining solvating ability of polymers and transport properties in gel-type polymer electrolytes. *Electrochim. Acta* **2000,** *45* (13), 2101-2109.
35. Ock, J.-y.; Fujishiro, M.; Ueno, K.; Watanabe, M.; Dokko, K., Electrochemical Properties of Poly(vinylidene fluoride-co-hexafluoropropylene) Gel Electrolytes with High-Concentration Li Salt/Sulfolane for Lithium Batteries. *Electrochemistry* **2021,** *89* (6), 567-572.
36. Sano, H.; Kitta, M.; Kubota, K., Impedance Analysis of the Side Reactions of Li Electrodeposition in a Quaternary Ammonium-Based Ionic Liquid Electrolyte. *Electrochemistry* **2024,** *92* (3), 037003.
37. Kühne, T. D.; Iannuzzi, M.; Del Ben, M.; Rybkin, V. V.; Seewald, P.; Stein, F.; Laino, T.; Khaliullin, R. Z.; Schütt, O.; Schiffmann, F.; Golze, D.; Wilhelm, J.; Chulkov, S.; Bani-Hashemian, M. H.; Weber, V.; Borštnik, U.; Taillefumier, M.; Jakobovits, A. S.; Lazzaro, A.; Pabst, H.; Müller, T.; Schade, R.; Guidon, M.; Andermatt, S.; Holmberg, N.; Schenter, G. K.; Hehn, A.; Bussy, A.; Belleflamme, F.; Tabacchi, G.; Glöß, A.; Lass, M.; Bethune, I.; Mundy, C. J.; Plessl, C.; Watkins, M.; VandeVondele, J.; Krack, M.; Hutter, J., CP2K: An electronic structure and molecular dynamics software package - Quickstep: Efficient and accurate electronic structure calculations. *J. Chem. Phys.* **2020,** *152* (19).
38. Perdew, J. P.; Burke, K.; Ernzerhof, M., Generalized Gradient Approximation Made Simple. *Phys. Rev. Lett.* **1996,** *77* (18), 3865-3868.
39. Grimme, S.; Ehrlich, S.; Goerigk, L., Effect of the damping function in dispersion corrected density functional theory. *J. Comput. Chem.* **2011,** *32* (7), 1456-1465.
40. Goedecker, S.; Teter, M.; Hutter, J., Separable dual-space Gaussian pseudopotentials. *Phys. Rev. B* **1996,** *54* (3), 1703-1710.
41. Nosé, S., A unified formulation of the constant temperature molecular dynamics

methods. *J. Chem. Phys.* **1984,** *81* (1), 511-519.
42. Hoover, W. G., Canonical dynamics: Equilibrium phase-space distributions. *Phys. Rev. A* **1985,** *31* (3), 1695-1697.
43. Martyna, G. J.; Klein, M. L.; Tuckerman, M., Nosé–Hoover chains: The canonical ensemble via continuous dynamics. *J. Chem. Phys.* **1992,** *97* (4), 2635-2643.
44. Martínez, L.; Andrade, R.; Birgin, E. G.; Martínez, J. M., PACKMOL: A package for building initial configurations for molecular dynamics simulations. *J. Comput. Chem.* **2009,** *30* (13), 2157-2164.
45. He, Y.; Ren, X.; Xu, Y.; Engelhard, M. H.; Li, X.; Xiao, J.; Liu, J.; Zhang, J.-G.; Xu, W.; Wang, C., Origin of lithium whisker formation and growth under stress. *Nat. Nanotechnol.* **2019,** *14* (11), 1042-1047.
46. Luo, J.; Fang, C.-C.; Wu, N.-L., High Polarity Poly(vinylidene difluoride) Thin Coating for Dendrite-Free and High-Performance Lithium Metal Anodes. *Adv. Energy Mater.* **2018,** *8*, 1701482.
47. Lu, R.; Shokrieh, A.; Li, C.; Zhang, B.; Amin, K.; Mao, L.; Wei, Z., PVDF-HFP layer with high porosity and polarity for high-performance lithium metal anodes in both ether and carbonate electrolytes. *Nano Energy* **2022,** *95*, 107009.
48. Yoshii, K.; Sakaebe, H., Lithium Metal Negative Electrode for Batteries with High Energy Density: Lithium Utilization and Additives. *Electrochemistry* **2020,** *88* (5), 463-467.
49. Homann, G.; Stolz, L.; Nair, J.; Laskovic, I. C.; Winter, M.; Kasnatscheew, J., Poly(Ethylene Oxide)-based Electrolyte for Solid-State-Lithium-Batteries with High Voltage Positive Electrodes: Evaluating the Role of Electrolyte Oxidation in Rapid Cell Failure. *Sci. Rep.* **2020,** *10* (1), 4390.
50. Klein, S.; Bärmann, P.; Beuse, T.; Borzutzki, K.; Frerichs, J. E.; Kasnatscheew, J.; Winter, M.; Placke, T., Exploiting the Degradation Mechanism of NCM523 Graphite Lithium-Ion Full Cells Operated at High Voltage. *ChemSusChem* **2021,** *14* (2), 595-613.
51. Maeyoshi, Y.; Miyamoto, S.; Munakata, H.; Kanamura, K., Enhanced cycle stability of LiCoPO4 by using three-dimensionally ordered macroporous polyimide separator. *J. Power Sources* **2017,** *350*, 103-108.

Table of Contents (TOC)